Supplementary Material For:

Single molecule FRET derived model of the synaptotagmin 1 – SNARE fusion complex

Ucheor B. Choi, Pavel Strop, Marija Vrljic, Steven Chu,
Axel T. Brunger and Keith R. Weninger

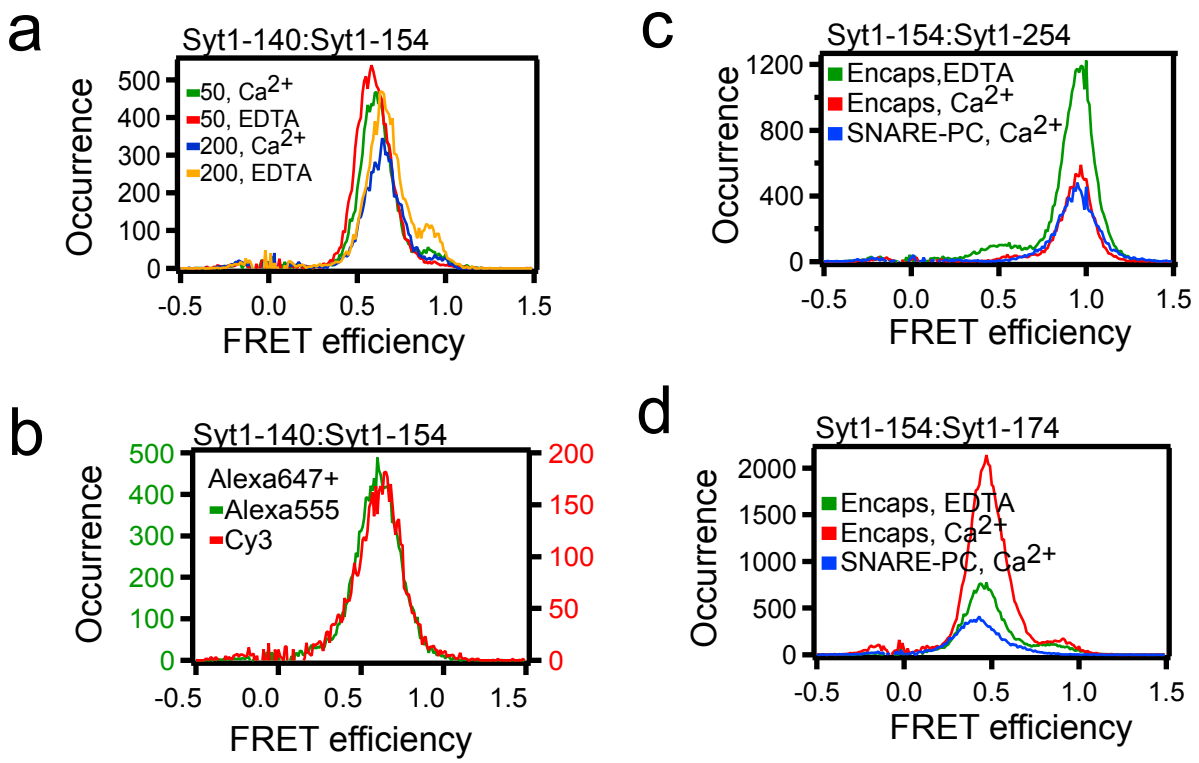

Supplementary Figure 1 FRET histograms for additional control experiments where both donor and acceptor are in the same C2A domain (see also Fig. 2d). (a) Liposome encapsulated experiments for Syt1 C2AB with labels at residues140 and 154 comparing 50 mM NaCl and 200 mM NaCl in the presence and absence of 1 mM CaCl2. (b) Compares experiments for Syt1 C2AB with labels at residues140 and 154 using Alexa555 to those using Cy3 as the donor dye for FRET measurements with Alexa647 as the acceptor for Syt1 bound to SNARE complexes in a lipid bilayer. (c) Additional control experiments using Syt1C2AB with labels at residues 154 and 254 or (d) Syt1 C2AB with labels at residues 154 and 174 under indicated conditions. 'Encaps' indicates vesicle encapsulation of Syt1. 'SNARE-PC' indicates binding of Syt1 to ternary SNARE complex reconstituted into 100% PC bilayers. EDTA or Ca^{2+} were present at 1 mM if indicated.

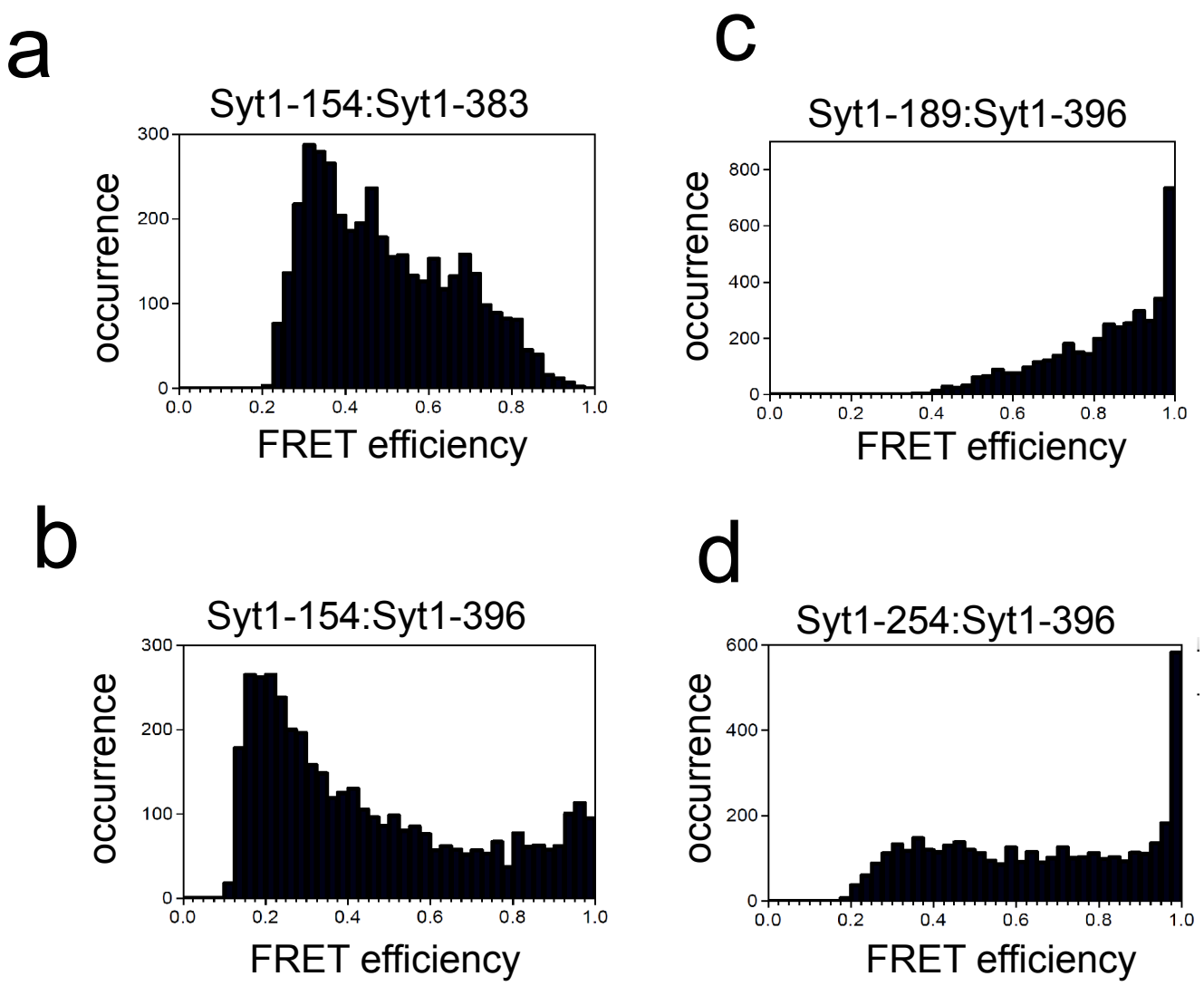

Supplementary Figure 2 Simulated FRET efficiency distributions using molecular dynamics simulations of Syt1 C2AB for the four C2AB spanning label pairs shown in Fig. 1c. The bin width in the histograms was set to 0.025.

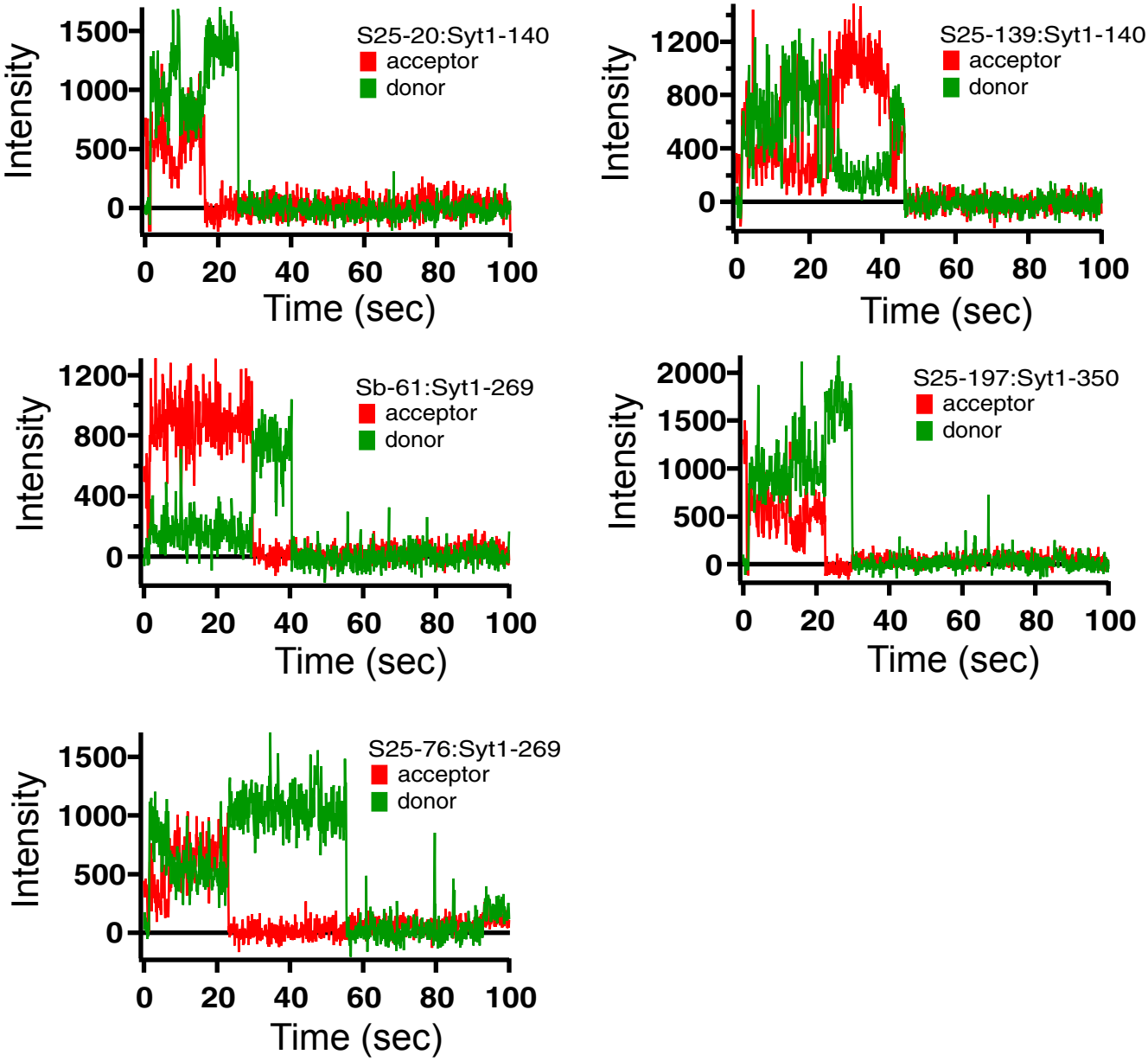

Supplementary Figure 3 Example traces showing transitions in FRET emission levels between a donor dye (Alexa555) on Syt1 and an acceptor dye (Alexa647) on the SNARE complex.

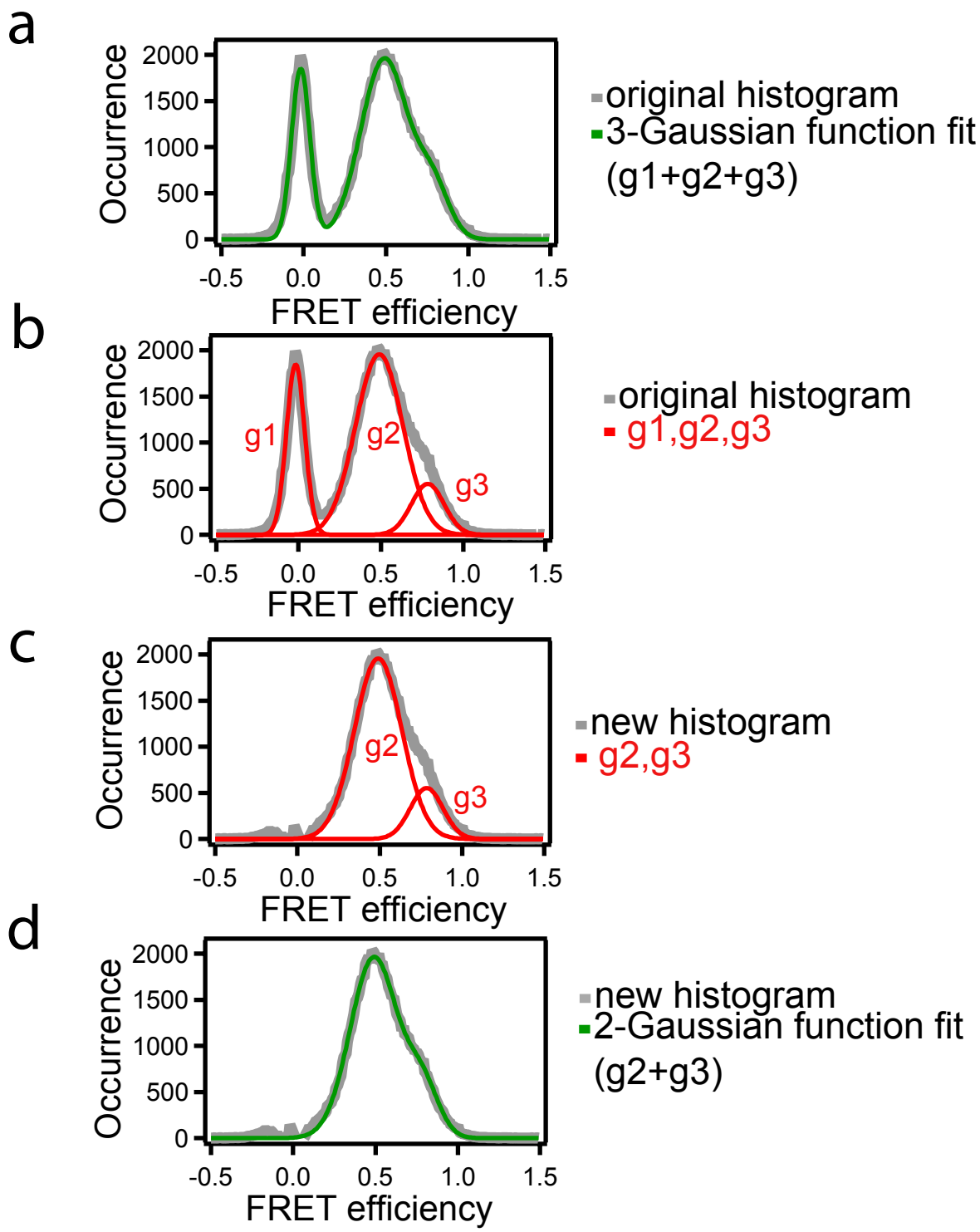

Supplementary Figure 4 Gaussian function fitting of smFRET distributions and zero FRET peak subtraction. The initial FRET histogram is fit to a sum of three Gaussian functions. All experiments contained a peak near FRET=0. This Gaussian fit function for the FRET=0 peak was subtracted from the smFRET efficiency distributions for further analysis. (a) Unprocessed histograms are displayed. In (b) the three Gaussian functions used as a sum to fit the data are shown. In (c) the FRET=0 fit Gaussian function has been subtracted from the data and the remaining two Gaussian fits are shown. Finally, in (d) the sum of the two remaining Gaussian functions is plotted against the processed data with the FRET=0 peak removed.

a

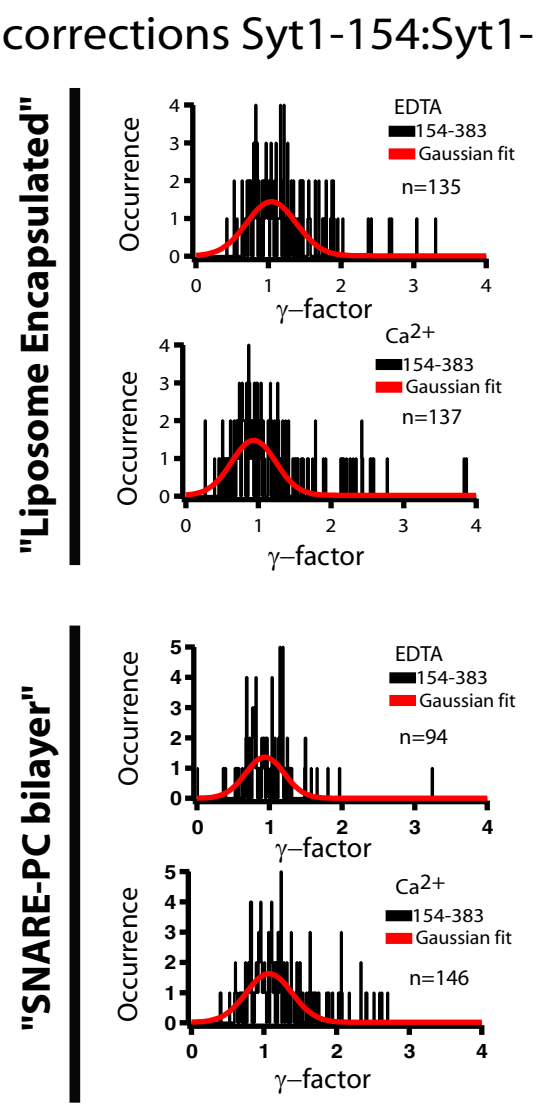

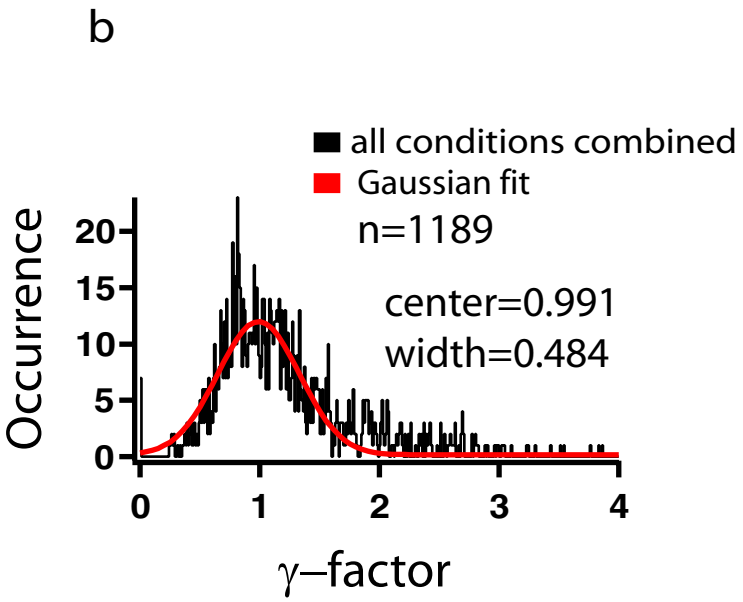

Supplementary Figure 5 Individual γ measurements for the labeling pair Syt1 154-383 with Alexa555:Alexa647 dyes in different conditions. γ values were measured from single molecule photobleaching events. a) shows histograms for indicated conditions. b) is an histogram formed by combining the individual experiments. Supplementary Table 1 lists more γ values derived from single molecule photobleaching events for additional label site combinations.

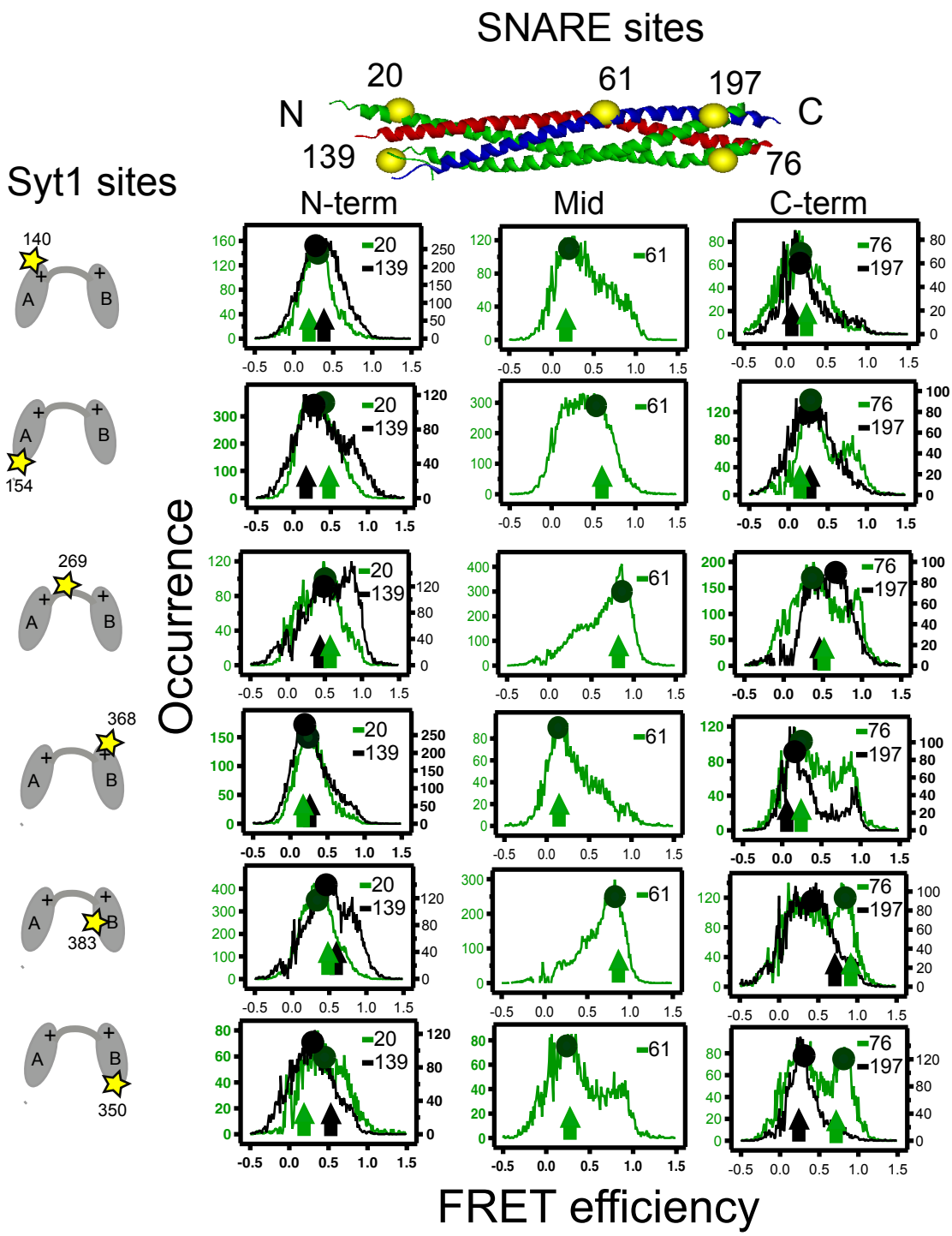

Supplementary Figure 6 Agreement of measured FRET efficiency distributions with calculated FRET from the best model of the Syt1 - SNARE complex. Circles indicate the FRET efficiency value used to derive a particular distance restraint for the docking calculations. The arrows indicate the value of FRET calculated from the model in Fig. 3c that results from converting the dye center - dye center distances into FRET efficiencies using R0=5.55 nm.

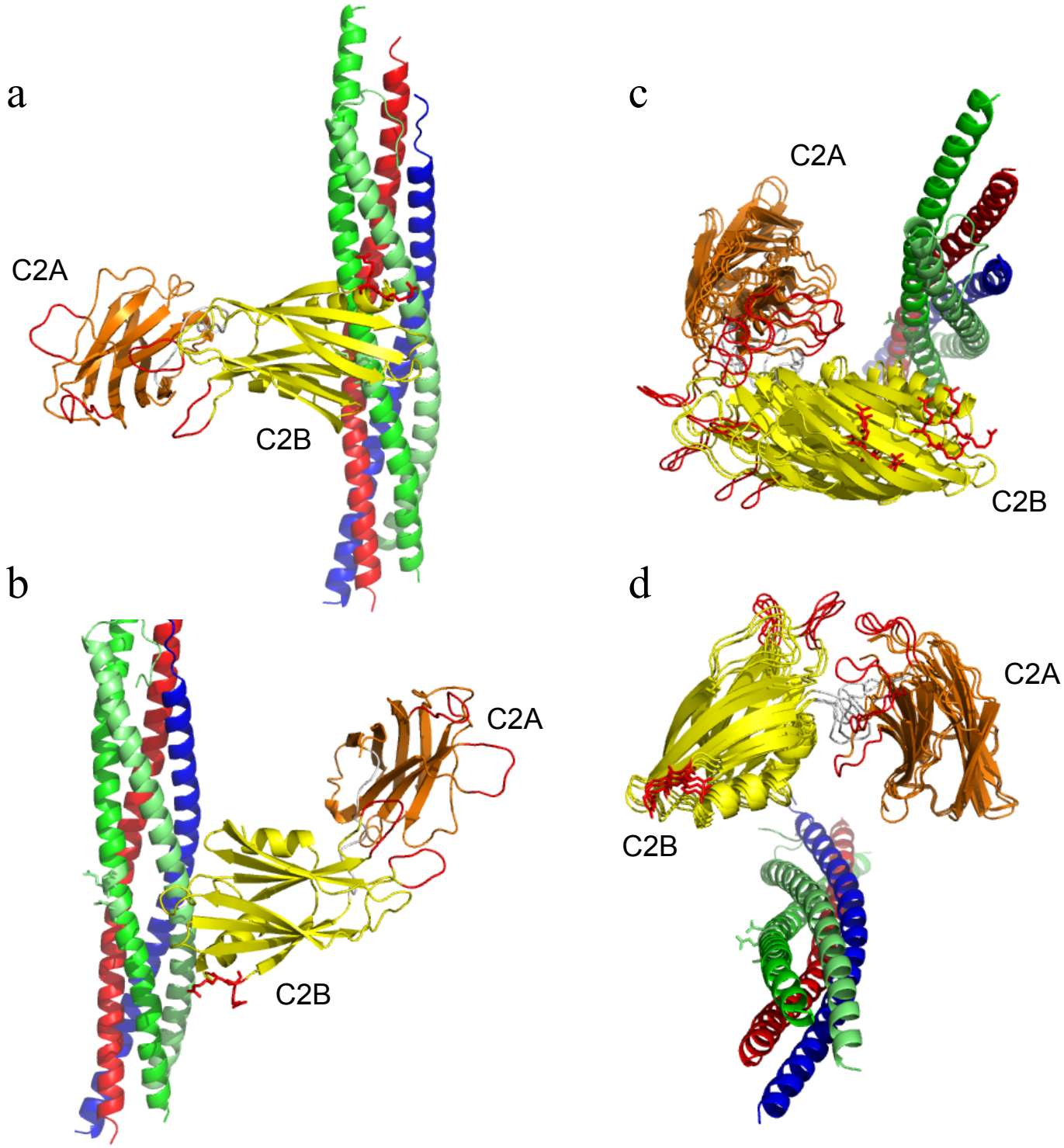

Supplementary Figure 7 Models 2 through 10 from the docking calculation. The distance satisfaction calculated by rmsdrd for the top ten models (after cluster analysis) are #1=0.383 (shown in Fig. 3c), #2=0.394, #3=0.400, #4=0.414, #5=0.417, #6=0.419, #7=0.422, #8=0.438, #9=0.449, #10=0.451 nm. (a) Showing model #5 which is qualitatively similar to the best model shown in Fig. 3c with an rmsd of 0.83 nm between the models. (b) Showing structure 7. Note that this conformation can be obtained from the best model (Fig. 3c) by a 180 degree rotation of the Syt1 molecule around an axis perpendicular to the superhelical axis of the SNARE complex. (c) Superposition of models # 2,3,4,6. (d) Superposition of models # 8, 9 and 10. For panels c and d, note the contacts between the Ca2+ binding loops of the C2A domain with the C2B domain. Thus, models 2,3,4,6, 8, 9, and 10 are physically unlikely. C2A is colored orange, C2B is yellow, SNAP-25 is green, synaptobrevin is blue, and syntaxin is red. The conserved arginine residues 398 and 399 in C2B are shown as red sticks, and the Ca2+ binding loops are colored red.

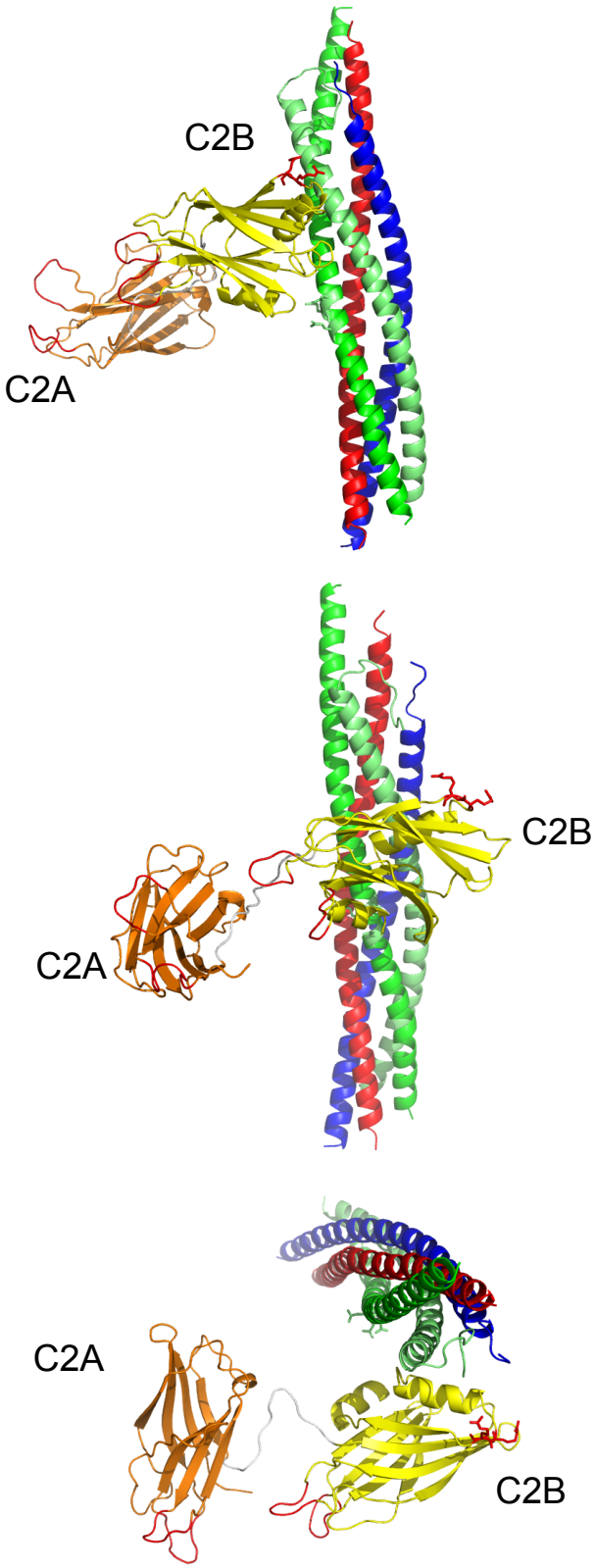

Supplementary Figure 8 Best model of the Syt1 - SNARE complex when the distance restraints using Syt1-383 label site are omitted. The same views are shown as for the model using all label sites (Fig. 3c). Note the similarity to the best model shown in Figure 3c using all 34 labeling pairs.C2A is colored orange, C2B is yellow, SNAP-25 is green, synaptobrevin is blue, and syntaxin is red. The conserved arginine residues 398 and 399 in C2B are shown as red sticks, and the Ca2+ binding loops are colored red.

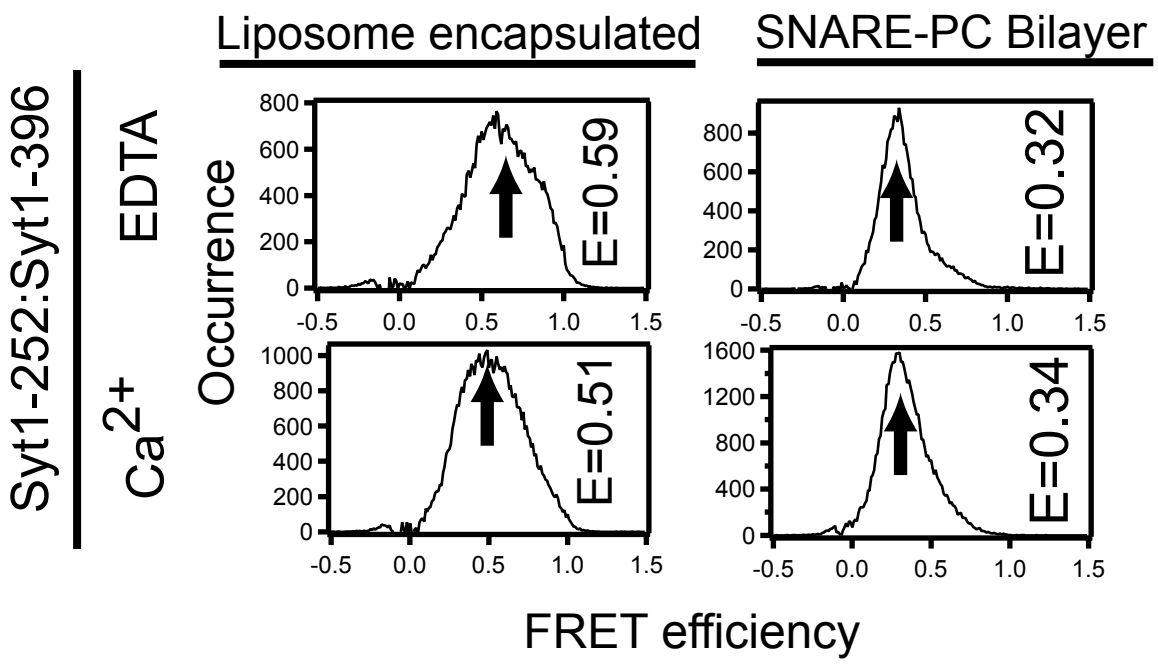

Supplementary Figure 9 smFRET efficiency histograms for the Syt1 C2AB construct with labels at residues 252 and 396. Conditions used are with (bottom) and without (top) Ca^{2+}, and liposome encapsulation (left) and supported bilayers (right). Arrows indicate the peak value (E) from Gaussian fits.

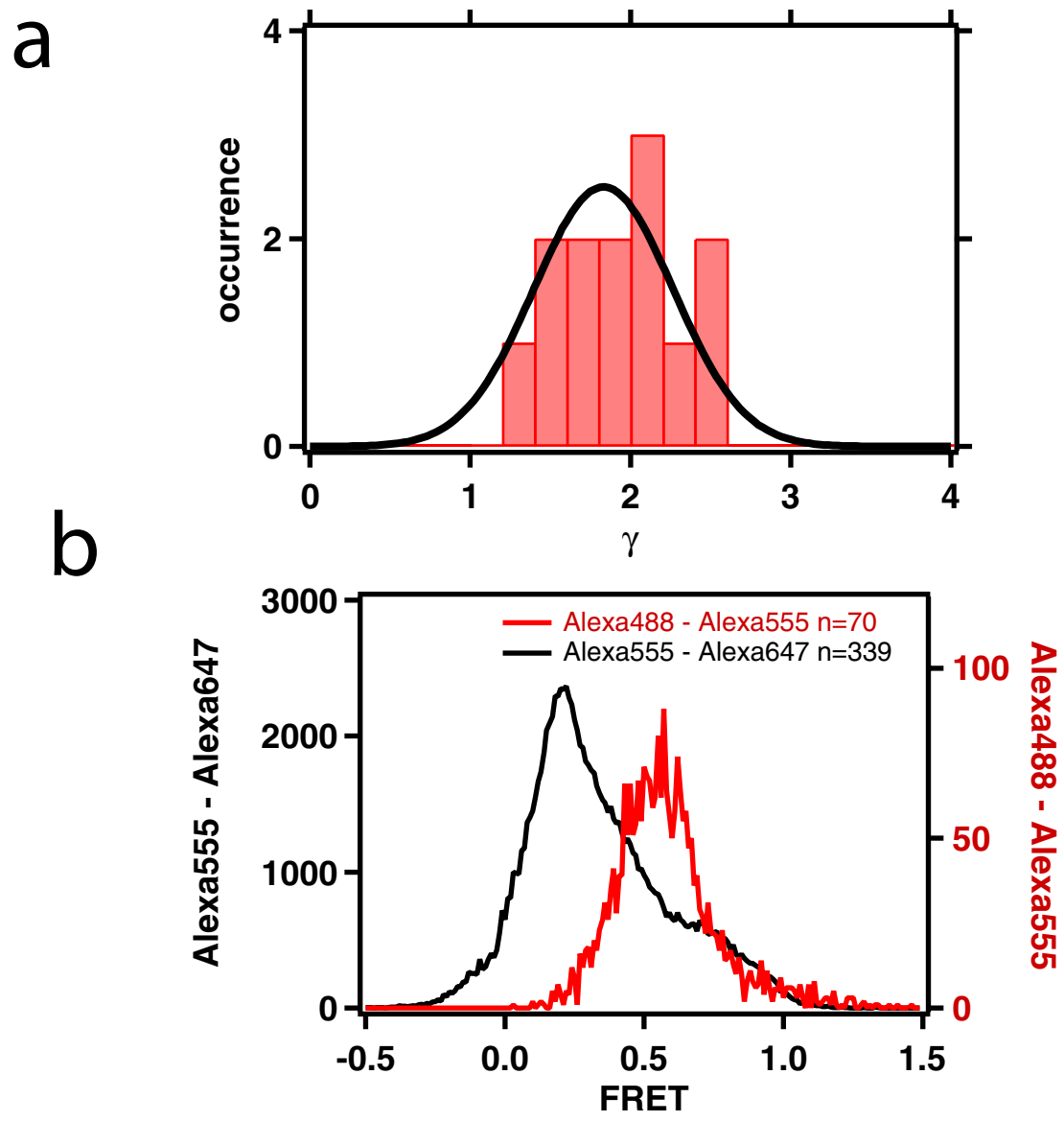

Supplementary Figure 10 FRET measurement for the Syt1 254:396 label pair using the Alexa488 and Alexa555 dye pair. a) γ factor measured from single molecule photobleaching events. A fit with a Gaussian function produces a center value of 1.83 whereas the mean value of the measured γ values is 1.92. b) In red is the FRET histogram (γ corrected with 1.83) from 70 molecules using the Syt1 254:396 label pair with Alexa488 and Alexa555 dyes. For comparison the FRET efficiency distribution for the same label site pair, but using Alexa555 and Alexa647 dyes (from Fig. 1c) is superimposed in black.

Supplementary Table 1: γ values for different sets of dye label attachment sites

label site A	**label site B**	**gamma**	**conditions**
Syt1-154	Syt1-383	0.93	Ca^{2+}; encapsulated
Syt1-154	Syt1-383	1.04	EDTA; encapsulated
Syt1-154	Syt1-383	1.07	Ca^{2+}; SNARE bilayer
Syt1-154	Syt1-383	0.94	EDTA; SNARE bilayer
Syt1-140	Syt1-154	0.92	EDTA; encapsulated
Syt1-140	Syt1-154	0.98	Ca^{2+}; encapsulated
Syt1-254	Syt1-396	0.97	Ca^{2+}; encapsulated
Syt1-254	Syt1-396	1.02	EDTA; encapsulated
Syt1-254	Syt1-396	0.89	Ca^{2+}; SNARE bilayer
Syt1-254	Syt1-396	1.04	EDTA; SNARE bilayer
Syt1-154	Syt1-174	1.06	Ca^{2+}; encapsulated
Syt1-368	Syt1-396	1.11	combined; encapsulated
Syt1-189	Syt1-396	1.16	Ca^{2+}; encapsulated
Sb-61	Syt1-383	0.97	Ca^{2+}; SNARE bilayer
S25-20	Syt1-269	0.95	Ca^{2+}; SNARE bilayer
S25-76	Syt1-140,269,350	0.83	Ca^{2+}; SNARE bilayer
S25-197	Syt1-368,350	0.85	Ca^{2+}; SNARE bilayer
S25-139	Syt1-140,154,269	0.94	Ca^{2+}; SNARE bilayer
	average	0.98	
	stdev	0.09	

Shown are the results of measurements of γ values for 23 labeling pairs with Alexa555:Alexa647 dyes. Although we did not measure γ values for all 34 pairs that were used in the docking calculations, the combinations that we used cover all label attachment sites used in this study.

Supplementary Table 2: Number of molecules contributing to smFRET efficiency distributions

Figure	label site	label site	# of molecules	Experiment	Condition
1c	154	383	425	liposome	EDTA
1c	154	383	319	liposome	Ca^{2+}
1c	154	396	75	liposome	EDTA
1c	154	396	101	liposome	Ca^{2+}
1c	189	396	230	liposome	EDTA
1c	189	396	147	liposome	Ca^{2+}
1c	254	396	447	liposome	EDTA
1c	254	396	339	liposome	Ca^{2+}
1c	154	383	197	SNARE bilayer	EDTA
1c	154	383	293	SNARE bilayer	Ca^{2+}
1c	154	396	74	SNARE bilayer	EDTA
1c	154	396	254	SNARE bilayer	Ca^{2+}
1c	189	396	27	SNARE bilayer	EDTA
1c	189	396	168	SNARE bilayer	Ca^{2+}
1c	254	396	103	SNARE bilayer	EDTA
1c	254	396	182	SNARE bilayer	Ca^{2+}
2c	154	383	319	liposome	Ca^{2+}
2c	154	383	97	liposome	BS3
2d	140	154	285	liposome	Ca^{2+}
2d	140	154	313	liposome	EDTA
2d	140	154	193	SNARE bilayer	Ca^{2+}
2d	140	154	97	SNARE bilayer	EDTA
4b	140	20	58	SNARE bilayer	Ca^{2+}
4b	154	20	41	SNARE bilayer	Ca^{2+}
4b	269	20	110	SNARE bilayer	Ca^{2+}
4b	368	20	49	SNARE bilayer	Ca^{2+}
4b	383	20	81	SNARE bilayer	Ca^{2+}
4b	350	20	47	SNARE bilayer	Ca^{2+}
4b	140	139	60	SNARE bilayer	Ca^{2+}
4b	154	139	133	SNARE bilayer	Ca^{2+}
4b	269	139	169	SNARE bilayer	Ca^{2+}
4b	368	139	105	SNARE bilayer	Ca^{2+}
4b	383	139	144	SNARE bilayer	Ca^{2+}
4b	350	139	35	SNARE bilayer	Ca^{2+}
4b	140	61	64	SNARE bilayer	Ca^{2+}
4b	154	61	138	SNARE bilayer	Ca^{2+}
4b	269	61	158	SNARE bilayer	Ca^{2+}
4b	368	61	49	SNARE bilayer	Ca^{2+}
4b	383	61	86	SNARE bilayer	Ca^{2+}
4b	350	61	36	SNARE bilayer	Ca^{2+}
4b	140	76	51	SNARE bilayer	Ca^{2+}
4b	154	76	90	SNARE bilayer	Ca^{2+}
4b	269	76	222	SNARE bilayer	Ca^{2+}
4b	368	76	74	SNARE bilayer	Ca^{2+}
4b	383	76	98	SNARE bilayer	Ca^{2+}
4b	350	76	35	SNARE bilayer	Ca^{2+}
4b	140	197	50	SNARE bilayer	Ca^{2+}
4b	154	197	98	SNARE bilayer	Ca^{2+}
4b	269	197	139	SNARE bilayer	Ca^{2+}
4b	368	197	38	SNARE bilayer	Ca^{2+}
4b	383	197	108	SNARE bilayer	Ca^{2+}
4b	350	197	52	SNARE bilayer	Ca^{2+}
S1a	140	154	285	liposome	50NaCl; Ca^{2+}
S1a	140	154	313	liposome	50NaCl; EDTA
S1a	140	154	30	liposome	200NaCl; Ca^{2+}
S1a	140	154	56	liposome	200NaCl; EDTA
S1b	140	154	285	liposome	Alexa555
S1b	140	154	28	liposome	Cy3
S1c	154	254	78	liposome	EDTA
S1c	154	254	44	liposome	Ca^{2+}
S1c	154	254	56	SNARE bilayer	Ca^{2+}
S1d	154	174	87	liposome	EDTA
S1d	154	174	182	liposome	Ca^{2+}
S1d	154	174	67	SNARE bilayer	Ca^{2+}
S2	252	396	180	liposome	Ca^{2+}
S4	252	396	95	SNARE bilayer	EDTA
S7	252	396	142	SNARE bilayer	Ca^{2+}
S9	252	396	208	liposome	EDTA

III. Supplementary Note

Control experiments with both donor and acceptor dyes in C2A, their implications, and label site selection: As control experiments we created C2AB constructs in which both the donor and acceptor were positioned within the C2A domain (Figs. 2a,b,d,e, and Supplementary Fig. 1). NMR studies have verified that both the C2A and C2B domain remain stably folded in isolation in a conformation nearly identical to that observed for each in the full C2AB fragment structures[23]. smFRET measurements of a control construct with label sites at residues 140 and 154 revealed a dominant peak centered around 0.60. In a few measurements there was a much smaller second peak (<10% of the population) near FRET~0.95 (Supplementary Fig. 1a). Such a high FRET peak is not consistent with any known structures of C2A. Dye interactions with the protein that might restrict full dye motion and alter the efficiency of FRET are not expected to lead to a unique high FRET state for multiple combinations of label sites (both for the C2A control and C2AB spanning FRET pairs). Furthermore, substitution of Cy3 for Alexa 555 in a control construct using label sites at residues 140 and 154 both in C2A did not change the FRET efficiency distribution (Supplementary Fig. 1b). One possible source of the high FRET state could be FRET between dyes on different synaptotagmin molecules that might dimerize in solution. The fact that the high FRET population is smaller when measuring this C2A FRET pair construct bound to SNARE complexes immobilized in lipid bilayers (Fig. 2d) suggests that if this is the source of the high FRET population then the multimeric synaptotagmin does not bind to the SNARE complex. In support of this notion, no high FRET population was observed for isolated Syt3 where the single molecules were immobilized on a surface[13].

If some fraction of the high FRET state in the C2AB fragment 154:383 FRET pair construct is caused by close proximity of the donor and acceptor in C2A and C2B, then we note that the high FRET state is consistent with the Ca^{2+} free Syt1 crystal structure[22] (Cα separation 2.7 nm) and the SNARE-induced Ca^{2+} bound Syt3 structure (Cα separation of aligned residues 317:546 is 2.7 nm). It is also incompatible with the Ca^{2+}-free Syt3 crystal structure (Cα separation of aligned residues 317:546 is 5.5 nm).

The selection of label sites requires careful consideration. For example, a dramatic shift of the maximum of the FRET efficiency distribution was observed for one label pair (252:396) when bound to the SNARE complex (Supplementary Fig. 9, compare "liposome encapsulated" and "SNARE-PC-bilayer" panels). The left-shift in FRET efficiency maximum might indicate that the labeled residues 252 and 396 of Syt1 move apart upon SNARE binding. However, in the available crystal structures of C2A, Phe252 is buried and is not surface accessible. Upon mutation to a cysteine, the linker to a reactive fluorophore would need to snorkel to the surface of the protein, possibly affecting the stability of the native conformation of C2A. Therefore, we discounted the FRET change for the 252:396 label pair. The 254 residue is oriented much more desirably and indeed the 254:396 label site pair does not show a large change of the peak position upon SNARE binding (Fig. 1c).

Subtraction of Gaussian peak due to acceptor bleaching: In assembling FRET histograms we included all intervals of non-zero FRET as well as a one second interval following the acceptor photobleaching for most molecules. The inclusion of the acceptor bleached intervals gives rise to a peak centered at FRET=0 that was present in all smFRET efficiency distribution of Syt1. This peak was well fit by a Gaussian function. Across all experiments, the average center of the Gaussian function was located at –0.00125 (st. dev. 0.0125) with an average width (σ) of 0.086 (st. dev. 0.0232), which is consistent with donor

only emission arising from acceptor bleaching and blinking (N=102) (Supplementary Fig. 4). The single Gaussian function fitting the zero FRET peak in each histogram that was derived from the three Gaussian function sum fit to the full data set was subtracted (Supplementary Fig. 4).

Simulation of dye center positions: Although the Cα coordinates for the cysteine mutations can be derived from the crystal structures of the C2A and C2B domains[15,17,22], they are separated from the dye center positions. In order to obtain more accurate dye-dye distances for the FRET analysis we generated an atomic model of a particular dye linked to the protein at the residue position used for labeling and calculated the mean dye position by performing a molecular dynamics simulation as described in detail in the accompanying paper[13]. Briefly, separate atomic models of the fluorophores and their maleimide linker attached to a particular residue in Syt1 or the SNARE complex were built and subjected to molecular dynamics simulations with all protein atoms fixed, but flexible dye and linker atoms. Approximately 500 simulations were performed for each labeling position and the average location of the center of the dye (CAO atom) was computed from the resulting coordinates. Cy3 and Cy5 were used as models for the dyes because the Alexa 555 structure is unavailable and the structures of Alexa 647 and Cy5 are very similar[45]. The linker in the Alexa maleimide and the Cy maleimide dyes are identical[13] suggesting that the dye center positions relative the reacted amino acid will be comparable. The resulting mean dye center positions protruded from the covalent attachment site in C2A, C2B or SNARE complex at an average distance from the Cα atom of the attachment residue of 0.97 nm (standard deviation 0.09 nm), a separation similar to that obtained by using other modeling approaches[9,10].

Determining R_o and γ for conversion of FRET to distance: The Förster theory that relates measured donor and acceptor intensities (I_D and I_A) to the dye-dye distance R is dependent on

two factors involving dye and instrument properties: R_o (the Förster Radius) and γ. R_o is the distance at which the efficiency of resonance energy transfer is 50% for a specific pair of fluorescent dyes. The γ factor combines the probabilities of the donor and acceptor fluorophores relax to the ground state from the fluorescent excited state by emitting a photon and the likelihood of experimentally detecting emitted photons as $\gamma=(\phi_A\eta_A)/(\phi_D\eta_D)$ where η is the instrumental detection efficiency and ϕ the dye quantum yield. The FRET efficiency (E) is experimentally determined as

$$E = 1/(1+\gamma(I_D/I_A)) \qquad (1)$$

and is related to the dye-dye distance R by

$$E= 1/(1+(R/R_o)^6) \; . \qquad (2)$$

We empirically determined γ for the Alexa555:Alexa647 dye pair using the method of single molecule photobleaching events[46] where $\gamma = \Delta I_A/\Delta I_D$ and ΔI are the intensity changes of the donor or acceptor intensities upon acceptor photobleaching. For specific pairs of labeling sites, we identified intensity timetraces where the acceptor dye photobleached before the donor dye photobleached (leading to anticorrelated intensity changes within a single 100 msec time interval as seen in the time traces in three of the four examples shown in Fig. 1b). The donor and acceptor intensities for these molecules were determined in the intervals before and after the photobleaching event (omitting the 0.5 seconds both immediately before and after the event, i.e., the intensity before the bleaching event at time = t is obtained by averaging the intensity from t–2 seconds to t–0.5 seconds and the intensity after the event is obtained by averaging the intensity from t+0.5 seconds to t+2 seconds). These averaged intensities were used to calculate the changes in donor and acceptor intensity upon bleaching (ΔI_D and ΔI_A), and $\gamma = \Delta I_A/\Delta I_D$. Distributions of γ factors for individual

measurements involving the Syt1-154:Syt1-383 label pair are shown in Supplementary Fig. 5 for the specified experimental conditions. The measured γ distributions for 15 other label pairs were similar. Gaussian fits to these distributions generally produced widths of ~0.4 and were centered near 1 (Supplementary Table 1). The mean center value for γ is 0.968 +/- 0.11. The similarity of the γ factors for all of the 16 different labeling pairs (covering all of the label sites used in this project) demonstrates that no specific site results in a significant change in critical dye parameters such as dye quantum efficiency, supporting the use of a single R_o parameter for all 34 label pairs used in the docking calculations. The results in Supplemental Table 1 also demonstrate that there is not a systematic difference in γ factor between the different experimental conditions: encapsulation vs. SNARE bound and EDTA vs. Ca^{2+}. We therefore used $\gamma = 1$ for our conversions of FRET efficiency to distance for the Alexa555:Alexa647 dye pair.

We used an empirical approach[47,48] to calibrate R_o for the Alexa555:Alexa647 dye pair by measuring the FRET efficiency for dyes attached to a single C2 domain of Syt1 with the dye separation deduced from the known crystal structure[22] and the molecular dynamics simulation of the mean dye center position described above. Three Syt1 label pairs were used with both label attachment sites within individual C2 domains: 140:154 and 154:174 (both pairs spanning C2A); and 368:396 (spanning C2B). Dye separations obtained from the molecular dynamics simulations based on the Syt1 crystal structure[22] were 5.4 nm (140:154), 5.9 nm (154:174), and 5.7 nm (368:396). We measured FRET efficiency from these label pairs (Figs. 2c,d and Supplementary Fig. 9) to be 0.60 (140:154), 0.41 (154:174), and 0.47 (368:396). These FRET efficiency measurements and calculated dye separations can be combined using $\gamma = 1$ to determine the calculated R_o for these label combinations as 5.78 nm

(140:154), 5.55 nm (154:174), and 5.58 nm (368:396). This can be compared to the theoretical R_o for the Alexa 555:Alexa647 dye pair of 5.1 nm[25]. R_o is expected to deviate from this published theoretical value due to changes in the dye microenvironment when conjugated to synaptotagmin. We selected the 154:174 result as the most reliable pair to determine R_o because residue140 is at the very beginning of the structured regions in C2A and thus might exhibit a bit more flexibility than residues deeper into the structured region, and FRET measurements of 368:396 were not repeated as often as for the 154:174 site, which was highly reproducible. The spread of the R_o values derived from our three different control constructs is 0.23 nm, which is smaller than the error bounds used in the docking calculation. Thus, the small uncertainty in the R_o value is unlikely to affect the docking calculations.

As a further check on the validity of our interpretation of FRET efficiency values, we compared results obtained from the same Syt1 labeling pair, but using two different pairs of fluorescent dyes with different values of R_0. Using Alexa555 and Alexa647, the measured FRET efficiency from liposome encapsulated Syt1 254:396 was on average 0.23 (Fig. 1c). This FRET efficiency corresponds to a dye-dye separation of 6.78 nm using the empirically determined $R_0 = 5.55$ nm and $\gamma = 1$ parameters for the Alexa555/Alexa647 dye pair. We then labeled the same Syt1 254:396 mutant instead with Alexa488 and Alexa555 in order to systematically shift the FRET efficiency. Table 1.6 in the Molecular Probes Handbook[25] gives a theoretical $R_0 = 7.0$ nm for this dye pair (compared to the theoretical R_0 of 5.1 for the Alexa55:Alexa647 pair in the same table). FRET efficiency measurements of Alexa 488:Alexa555 labeled Syt1 254:396 encapsulated in liposomes were made using the same experimental conditions as in Fig. 1c with the following changes: a 473 nm laser was used for excitation, a 565dcrx dichroic mirror (Chroma Inc.) was used to split donor and acceptor

emission, and HQ507x30m and HQ630x120m emission filters (both Chroma Inc.) were used in the donor and acceptor paths respectively. For these optical filters, the donor leakage into the acceptor channel was 35% (which was corrected during data processing). Using the method of analyzing single molecule photobleaching events described above, we experimentally determined the γ factor for these Syt1:Alexa488-Alexa555 experiments to be 1.83 (Supplementary Fig. 10a). We applied $\gamma = 1.83$ to correct the measured FRET efficiency from Alexa488:Alexa555 labeled Syt1 254:396 and obtained FRET = 0.55 (Supplementary Fig. 10b). Using the dye-to-dye distance derived from the Alexa555:Alexa647 measurement of this label pair (6.78 nm, using the empirical R_0 of 5.55 nm) along with the Alexa488-Alexa555 measured FRET efficiency yields an empirical R_0 for the Alexa488:Alexa555 pair of 7.02 nm. Observing the expected shift in FRET efficiency upon changing to the new pair of dyes lends confidence to our calibration scheme for R_0.

FRET efficiency distribution calculated for C2AB assuming random motion between domains: Extensive (2 nsec) torsion angle molecular dynamics of the C2A-C2B fragment of Syt1 were performed with the two C2 domains treated as rigid bodies (residues 140:262 and 273:418, respectively), while the torsion angles of the linker (residues 263-272) connecting the two domains were kept variable (Supplementary Fig. 2). Pseudoatoms were rigidly associated with the C2 domains at the indicated labeled residue positions. The position of the pseudoatom relative to the rigid bodies was derived from the simulated dye center positions. Only repulsive van der Waals energy terms were included in the simulation. An extended van der Waals radius of 0.5 nm is used for the pseudoatoms. The simulations were performed in vacuum for 2 nsec with a timestep of 0.005 psec at 300 K. This is not meant to be a realistic simulation which would require inclusion of solvent and electrostatics but rather to provide information about the range of possible conformations of Syt1. Distances for the four dye

pairs listed in Fig. 1c were sampled every 100 molecular dynamics steps. Distances (R) were converted to FRET efficiencies (E) with R_o set to 5.55 nm using,

$$E = 1/(1+(R/R_o)^6). \quad (3)$$

Docking calculations for the smFRET-derived model of the Syt1 - SNARE complex: To dock synaptotagmin C2AB fragments to the SNARE complex we used rigid body molecular dynamics guided by smFRET derived distance restraints (Fig. 4b). This docking method is reminiscent to other rigid body docking methods described previously [49,50]. The SNARE complex, and the two C2 domains were treated as independent rigid bodies (residues 140:262 and 273:418, respectively), while the torsion angles of the linker connecting the two domains (residues 263-272) was simulated in torsion angle space, i.e., with bond lengths and bond angles fixed. The dyes center positions were simulated as pseudoatoms with their positions derived from the simulated dye center positions described above. The pseudoatoms were rigidly associated with their respective C2 domains at the indicated labeled residue positions. The coordinates for the SNARE complex were obtained from the crystal structure of the neuronal SNARE complex (PDB ID 1SFC)[38] and those of the C2 domains of Syt1 from the Ca^{2+}-free crystal structure of Syt1 (PDB ID 2R83)[22].

30,000 steps of molecular dynamics[51] at 2,000 K were performed with a time step of 0.001 psec, followed by a linear slow-cooling to 0 K with a cooling rate of 12.5 K / 6 steps. 1000 trials with different randomly assigned orientations of the C2AB fragment, different relative conformations of the C2 domains, and initial velocities were performed for each set of calculations. smFRET-derived distance restraints employed a harmonic square-well potential applied to the dye center pseudoatom positions[52]. The total energy function consisted of a repulsive term for the nonbonded interactions (i.e., excluding electrostatic and attractive van der Waals terms) and the distance restraints term[53]. This type of energy

function is widely used for three-dimensional structure determination based on nuclear Overhauser effect (NOE) derived distances using multi-dimensional nuclear magnetic resonance spectroscopy (NMR)[54]. The smFRET distributions between Alexa555-labeled synaptotagmin 1 C2AB fragment and Alexa647-labeled ternary SNARE complex were converted to distances as described above. FRET becomes less sensitive to dye separation at distances much less and much greater than R_o (see equation (1)). Therefore, we used bounds for the square well potential as ±0.25 nm around the FRET-derived distance ($d_{i,measuredFRET}$) for label combinations yielding FRET efficiency values between 0.25 and 0.75, and ±0.5 nm for those with values outside this range. All molecular dynamics calculations were performed using the Crystallography and NMR System (CNS)[55].

Each solution was characterized by the root mean squared (rms) deviation between the distances predicted by the model and the distance ranges used as the square well potentials derived from the FRET measurements involving the 34 label pairs. If for the i^{th} label pair the square well potential was centered on $d_{i,measuredFRET}$ and spanned a range of distances between $d_{i,lower\ well\ edge}$ and $d_{i,upper\ well\ edge}$, then we calculated Δ_i as the deviation of the model predicted distance between the dye centers ($d_{i,model}$) and this potential well as,

$$\Delta_i = 0 \quad , \text{if } d_{i,lower\ well\ edge} < d_{i,model} < d_{i,upper\ well\ edge} \tag{5}$$

$$\Delta_i = (d_{i,upper\ well\ edge} - d_{i,model}) \quad , \text{if } d_{i,model} > d_{i,upper\ well\ edge} \tag{6}$$

$$\Delta_i = (d_{i,lower\ well\ edge} - d_{i,model}) \quad , \text{if } d_{i,model} < d_{i,lower\ well\ edge} \ . \tag{7}$$

From this set of Δ_i we formed a quantity designated the root mean squared distance range deviations (rmsdrd) from the formula

$$\text{rmsdrd} = \sqrt{\frac{1}{34}\sum_{i=1}^{34}(\Delta_i)^2} \ . \tag{8}$$

The solutions of the docking simulations were sorted by rmsdrd satisfaction in increasing order. The solutions were superimposed with respect to the SNARE complex. The solutions were then clustered according to the root-mean-square difference (rmsd) between C2AB conformations (using 0.3 nm as the maximum distance between the central node of the cluster and all members of the cluster) using an algorithm implemented in the program HADDOCK[56]. For each cluster, the structure with the best distance satisfaction (rmsdrd) was used for further analysis.

Some of the 34 distance restraints involved multiple distinct FRET populations (Fig. 4b). Therefore, the docking calculations proceeded in two steps. FRET efficiency distributions were analyzed by fitting to sums of two or more Gaussian functions (Supplementary Fig. 4). For 26 of the 34 measured FRET pairs, the major fitted peaks capture 70% or more of the total non-zero smFRET distribution; ten label pairs have distributions with a major peak comprising 90% of the total distribution, seven label pairs between 90% and 80%, nine between 80% and 70%. The assignments of the dominant FRET states at the 70% level were robust against run-to-run variation. Repeating measurements of single label pair combinations generated the same central FRET efficiency values within experimental error for all label pairs and for most label pairs the dominant population was consistently above the 70% value. For all pairs the dominant population was observed at levels above 70% in at least 66% of the repeated experiments. Many were confirmed greater than 70% dominant in all repeats. One of the few examples without perfect run to run repeatability of the dominant population above the 70% rule is the Syt1-269:SNAP-25-139 label pair: in four repeated experiments a sum of two-Gaussian function fit the FRET efficiency distributions with the following set of parameters -- low FRET population peak position [0.46, 0.53, 0.47, 0.44]; high FRET population peak position [0.88,

0.85, 0.80, 0.84]; low FRET peak % population [77%, 78%, 51%, 83%]; high FRET peak % population [23%, 22%, 49%, 17%].

For final modeling we pooled all of the repeated experiments for each label pair into a single histogram to address the most probably configuration observed across multiple repeated experiments (at least three repeats for every label site pair). For label pairs with FRET efficiency distributions with a dominant peak of >70% of the total area, the FRET measurements were converted to distances and used as restraints for a first round of docking calculations (26 out of 34 pairs were included at this first step). The FRET histograms for the remaining eight label combinations (synaptobrevin-61:Syt1-140, synaptobrevin-61:Syt1-154, synaptobrevin-61:Syt1-269, synaptobrevin-61:Syt1-368, synaptobrevin-61:Syt1-383, SNAP-25-76:Syt1-154, SNAP-25-76:Syt1-350, SNAP25-76:Syt1-383) required sums of two Gaussian functions to fit where neither comprised more than 70% of the total population. These measured distances were compared to the best model from the first simulation using the first 26 distances and the measured distance that was closer to the model distance was selected. Then the simulation was repeated using all 34 restraints. The resulting models did not change significantly upon inclusion of the eight additional restraints.

Supplementary Fig. 7 shows the ten best models sorted by rmsdrd (Eq. 8). The best model shown in Fig. 4c (and a qualitatively similar model (#5) among the top ten solutions, Supplementary Fig. 7a) appeared consistently as the best cluster (with respect to distance satisfaction) for a number of docking calculations using several approaches to interpret the observed FRET efficiency distributions. A different possible model is shown in Supplementary Fig. 7b. This particular model approximately involves the same regions of the Syt1 and the SNARE complex facing each other (except for a 180 degree rotation). However, the poorer distance satisfaction along with the somewhat wider separation between

Syt1 and the SNARE complex make this second solution somewhat less likely than the top model. The other models among the top ten solutions (2,3,4,6,8,9,10) are all physically unlikely since they involve contacts between the Ca^{2+} binding loops of the C2A domain with the C2B domain (Supplementary Figs. 7c,d).

Supplementary Fig. 6 displays the FRET efficiency distributions for all label pairs along with the target distance values used as the input to the docking calculations (circles) and the FRET efficiency values calculated from the best model (arrows). Table 1 compares the FRET-derived target distances to the distances between dye centers calculated from the best model. The agreement is generally very good, except for a few cases. Some of the outliers coincide with the most unusual, non-Gaussian smFRET distributions (e.g., label pairs Syt1-350:SNAP-25-20, Syt1-383:SNAP-25-197, Syt1-269:SNAP-25-197 and Syt1-269:SNAP-25-76).

We also performed a docking simulation using the minor populations from each of the FRET label distances (if only one FRET population was present, it was used for both the major and minor population simulation) but convergence was much poorer than the major populations. Further, in the top solutions with the minor FRET populations the Ca^{2+} binding loops of C2A and C2B are interacting, making them unavailable for membrane binding. Thus, the conformations arising from docking using the major FRET population restraints are much more likely to occur than those derived using the minor FRET populations.

Uniformly increasing or decreasing all major FRET derived distance restraints by 1 nm led to non-physical results where the proteins were far away from each other or overlapped in space respectively. If the intra-C2 domain restraints were released then the models converged to the same C2B docking state, but the location of C2A became variable.

For the best model the dye attached at the Syt1-383 site is positioned near the binding interface with the SNARE complex. We therefore repeated the docking calculations omitting all of the restraints that involved the Syt1-383 site (Supplementary Fig. 8). Remarkably, the resulting top model was very similar to the docking calculation using all distances (compare Fig. 4c to Supplementary Fig. 8) with the only significant difference being that Syt1 was slightly closer to the SNARE complex. The observation that the models do not directly touch each other is a limitation of the approximations used in the docking calculations since there may be changes of the molecule's conformation or dye positions that are not taken into account in these calculations. Because the number of restraints far exceeds the number of degrees of freedom for our docking calculations, it is reasonable that omitting a few restraints does not lead to drastically different solutions. The similarity of the top models with and without distances involving the Syt1-383 sites illustrates the robustness of the top solution with respect to such cross-validation.

IV. Supplementary References

45. White, S.S. et al. Characterization of a single molecule DNA switch in free solution. *Journal of the American Chemical Society* **128**, 11423-11432 (2006).
46. Ha, T. et al. Single-molecule fluorescence spectroscopy of enzyme conformational dynamics and cleavage mechanism. *Proc Natl Acad Sci U S A* **96**, 893-8 (1999).
47. Amir, D. & Haas, E. Estimation of intramolecular distance distributions in bovine pancreatic trypsin inhibitor by site-specific labeling and nonradiative excitation energy-transfer measurements. *Biochemistry* **26**, 2162-75 (1987).
48. Amir, D. & Haas, E. Reduced bovine pancreatic trypsin inhibitor has a compact structure. *Biochemistry* **27**, 8889-93 (1988).
49. Dominguez, C., Boelens, R. & Bonvin, A.M. HADDOCK: a protein-protein docking approach based on biochemical or biophysical information. *J Am Chem Soc* **125**, 1731-7 (2003).
50. Schwieters, C.D. & Clore, G.M. Internal coordinates for molecular dynamics and minimization in structure determination and refinement. *J Magn Reson* **152**, 288-302 (2001).

51. Rice, L.M. & Brunger, A.T. Torsion angle dynamics: reduced variable conformational sampling enhances crystallographic structure refinement. *Proteins* **19**, 277-90 (1994).
52. Brunger, A.T. *X-PLOR, version 3.1. a system for X-ray crystallography and NMR*, (Yale University Press, New Haven, 1992).
53. Engh, R.A. & Huber, R. Accurate Bond and Angle Parameters for X-Ray Protein-Structure Refinement. *Acta Crystallographica Section A* **47**, 392-400 (1991).
54. Brunger, A.T. & Nilges, M. Computational challenges for macromolecular structure determination by X-ray crystallography and solution NMR-spectroscopy. *Q Rev Biophys* **26**, 49-125 (1993).
55. Brunger, A.T. et al. Crystallography & NMR system: A new software suite for macromolecular structure determination. *Acta Crystallogr D Biol Crystallogr* **54**, 905-921 (1998).
56. de Vries, S.J. et al. HADDOCK versus HADDOCK: new features and performance of HADDOCK2.0 on the CAPRI targets. *Proteins* **69**, 726-33 (2007).